



# Fabrication of a ternary plasmonic photocatalyst of Ag/AgVO<sub>3</sub>/RGO and its excellent visible-light photocatalytic activity

Wei Zhao<sup>a</sup>, Jinhai Li<sup>a</sup>, Zhong bo Wei<sup>a</sup>, Shaomang Wang<sup>a</sup>, Huan He<sup>a,b,\*</sup>, Cheng Sun<sup>a,\*</sup>, Shaogui Yang<sup>a,c</sup>

<sup>a</sup> State Key Laboratory of Pollution Control and Resource Reuse, School of the Environment, Nanjing University, Nanjing 210023, PR China

<sup>b</sup> School of Public Health, University of Illinois at Chicago, Chicago, IL 60631, United States

<sup>c</sup> Department of Plant, Soil and Microbial Sciences, Michigan State University, East Lansing, Michigan 48824, United States

## ARTICLE INFO

### Article history:

Received 4 March 2015

Received in revised form 26 April 2015

Accepted 1 May 2015

Available online 5 May 2015

### Keywords:

Hydrothermal method  
Plasmonic photocatalyst  
Bisphenol A

## ABSTRACT

The novel ternary plasmonic photocatalyst was successfully fabricated for the first time through a facile one-step in-situ hydrothermal method, in which the crystallization of AgVO<sub>3</sub>, Ag nanoparticles generated from AgNO<sub>3</sub> decomposition and reduction of graphene oxide (GO) to reduced graphene oxide (RGO) were achieved simultaneously. The as-obtained Ag/AgVO<sub>3</sub>/RGO ternary plasmonic photocatalyst exhibits excellent light-trapping ability and photocatalytic performance, which can be attributed to the enhanced absorbance in the visible light region, the good adsorptive capacity to organic molecules, the small widths of the Ag/AgVO<sub>3</sub> nanoribbons, the facilitated charge transfer and the suppressed recombination of electron–hole pairs in Ag/AgVO<sub>3</sub>/RGO. The photocatalytic mechanism over Ag/AgVO<sub>3</sub>/RGO ternary plasmonic photocatalyst was discussed in detail. Five intermediates and products formed in the photocatalytic degradation of Bisphenol A were also identified by the Gas Chromatography–Mass Spectrometer.

© 2015 Elsevier B.V. All rights reserved.

## 1. Introduction

Development of highly efficient photocatalysts for the solar energy conversion and the elimination of organic pollutants has been considered to be one of the important investigative fields [1–5]. TiO<sub>2</sub>, a traditional photocatalyst, has been widely investigated due to its optical and electronic properties, low cost, nontoxicity and relatively high chemical stability. However, the TiO<sub>2</sub> photocatalyst cannot be widely used in practical applications yet because of the relatively wide band gap and the limited visible-light absorption. Therefore, numerous new photocatalysts with appropriate band edge positions have been designed and explored to make full use of the solar energy [6–8]. Particularly, since Zou et al. [9] reported direct splitting of water under visible-light irradiation with new types of oxide semiconductor photocatalyst, visible-light-driven photocatalyst has become one of the hot spots in the field of photocatalysis research [10,11].

In the recent past, AgVO<sub>3</sub> materials have received much attention because of their potential applications in rechargeable high-energy density lithium batteries [12], sensors [13] and photocatalysts [14–19]. Besides, the unique hybridized valence bands (V 3d, O 2p, and Ag 4d orbitals) lead to a narrow band gap and highly dispersed valence bands, which makes it a potential application as visible-light-sensitive photocatalyst [20]. However, the photocatalytic activity of AgVO<sub>3</sub> is still low due to its poor capability to separate electron–hole pairs. Thus, further study is necessary to enhance its performance for the practical application.

An effective way to enhance the photocatalytic activity of catalyst is to construct specific nanostructured architectures with various dimensions, including zero-, one-, two-, and three-dimensional (0-D, 1-D, 2-D, and 3-D) nanomaterials, owing to their unique size- and/or shape-dependent physicochemical properties. Therefore, considerable efforts have been made to fabricate AgVO<sub>3</sub> with different morphologies [21]. For instance, Bao et al. [22] reported a novel channel structured β-AgVO<sub>3</sub>. Yu et al. [23] developed a simple approach for high-yield synthesis of β-AgVO<sub>3</sub> nanoribbons. 1-D AgVO<sub>3</sub> nanoribbon exhibits excellent photocatalytic performance among these morphologies because it has a large aspect ratio, which favors a directional charge transport with a reduced grain boundary and promotes their photocatalytic activity.

\* Corresponding authors at: State Key Laboratory of Pollution Control and Resource Reuse, School of the Environment, Nanjing University, Nanjing 210023, PR China. Tel.: +86 25 89680258; fax: +86 25 89680580.

E-mail addresses: [hhdeu@nju.edu.cn](mailto:hhdeu@nju.edu.cn) (H. He), [envidan@nju.edu.cn](mailto:envidan@nju.edu.cn) (C. Sun).

In addition, the high efficient plasmonic photocatalysts silver/silver halide ( $\text{Ag}/\text{AgX}$ ,  $\text{X} = \text{Cl}, \text{Br}$ ) have attracted much attention recently [24]. This has given us enlightenment: similarly, the photocatalytic activity of  $\text{AgVO}_3$  would be greatly improved if the silver modification on the surface of the sample [25]. The charge transfer between semiconductor and Ag substantially improves the separation of electrons and holes as Ag has the excellent conductivity and strong electron trapping ability. Moreover, the nanostructures of the modified Ag can induce localized surface plasmon resonance (SPR) from the collective oscillation of the surface electrons and they exhibit a great potential to extend the light-absorption range of semiconductors [26,27]. Some studies have reported that SPR can extend the photoresponse of catalysts and enhance charge separation, which in turn improves the catalytic performance [28,29]. Long et al. have reported that SPR can not only harvest visible light and convert them to free energetic electrons, but also promote the electron-hole pair formation rate driven by the electromagnetic field formed nearby the semiconductor [30]. Wang et al. [31] have developed a series of  $\text{Ag}@\text{AgX}$  plasmonic photocatalysts, which are highly efficient and stable under visible-light illumination. Lin et al. have reported that the  $\text{Ag}@\text{Ag}_3(\text{PO}_4)_{1-x}\text{-ZnO}$  hybrid nanoelectrodes exhibit the strong photooxidative capabilities to evolve  $\text{O}_2$  from  $\text{H}_2\text{O}$  [32]. More importantly, a highly stable performance of  $\text{AgVO}_3$  could be obtained as the Ag particles have already been formed and can act as photogenerated electron traps by removing electrons from the irradiated  $\text{AgVO}_3$  [33].

Recently, graphene oxide (GO) and reduced graphene oxide (RGO) have received much attention owing to its several exceptional properties, such as high chemical and thermal stability, large specific surface area, and high electron mobility [34]. Considering these excellent properties, 2-D GO or RGO nanosheets could have been recognized as one of the most ideal candidates as catalyst carrier or promoter [35]. In the photocatalysis reactions, it is proved that GO or RGO can facilitate the separation process of photogenerated electrons and holes, resulting in a high photocatalytic activity. For example, Jiang et al. have designed a novel  $\text{Ag}/\text{Ag}_3\text{PO}_4/\text{graphene}$  triple heterostructure, which exhibits high catalytic activity and structural stability under visible-light irradiation [36]. Zhu et al. [37] have reported that well-defined GO enwrapped  $\text{Ag}/\text{AgX}$  ( $\text{X} = \text{Br}, \text{Cl}$ ) composites can be facilely fabricated via a water/oil system. Compared with the corresponding bare  $\text{Ag}/\text{AgX}$  nanospecies, the GO-involved composites ( $\text{Ag}/\text{AgX}/\text{GO}$ ) display distinctly enhanced photocatalytic activities.

On the basis of the above investigations, it seems logical that one of the ideal ways to fabricate the highly efficient photocatalysts may be to combine these approaches together, that is, 1-D plasmonic nanostructures hybridized with 2-D nanosheets. As a matter of fact, by taking advantage of the above-mentioned merits of 1-D  $\text{Ag}/\text{AgVO}_3$  nanoribbons and 2-D RGO nanosheets, it is strongly desired that highly efficient photocatalysts are realized by hybridization of these components. However, until now, there is few report focusing on the assembly of 2-D RGO nanosheet with 1-D  $\text{Ag}/\text{AgVO}_3$  nanoribbon.

Herein, we report for the first time the successful attempt at the fabrication of  $\text{Ag}/\text{AgVO}_3/\text{RGO}$  ternary plasmonic photocatalyst through a facile one-step in-situ hydrothermal method (Fig. 1), in which the crystallization of  $\text{AgVO}_3$ , Ag nanoparticles generated from  $\text{AgNO}_3$  decomposition and reduction of GO to RGO were achieved simultaneously. In this innovative hybrid structure, 1-D  $\text{Ag}/\text{AgVO}_3$  nanoribbons should be uniformly dispersed on 2-D RGO nanosheet surfaces. The as-obtained  $\text{Ag}/\text{AgVO}_3/\text{RGO}$  ternary plasmonic photocatalyst would exhibit excellent light-trapping ability and catalytic performance. Our work might open up new possibilities for the development of highly efficient visible-light-driven plasmonic photocatalysts for the degradation of organic pollutants.

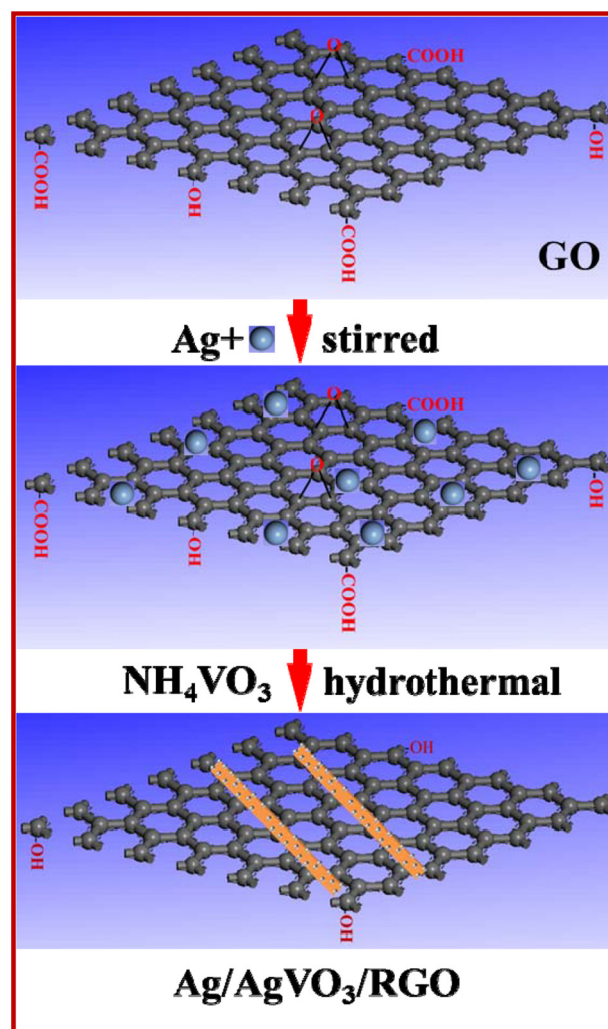


Fig. 1. Schematic of the synthesis of  $\text{Ag}/\text{AgVO}_3/\text{RGO}$  ternary plasmonic photocatalyst.

## 2. Experimental

### 2.1. Materials

Silver nitrate ( $\text{AgNO}_3$ ), ammonium metavanadate ( $\text{NH}_4\text{VO}_3$ ), graphite and other chemicals used in the experiments were of analytically pure grade (99%). These chemicals were purchased from Shanghai Chemical Reagent Ltd., without further purification. Deionized water was used throughout this study.

### 2.2. Preparation of 1-D $\text{AgVO}_3$ and $\text{Ag}/\text{AgVO}_3$ nanoribbons

The  $\text{AgVO}_3$  nanoribbons were synthesized through a facile hydrothermal process. In a typical procedure, the solution of  $\text{AgNO}_3$  (0.050 mol/L, 20 mL) was stirred for 30 min. After that,  $\text{NH}_4\text{VO}_3$  (0.050 mol/L, 20 mL) was added to form the suspension, which was stirred magnetically for 180 min. The resulted mixture was transferred into a Teflon-lined stainless-steel autoclave with a volume capacity of 100 mL. It was sealed and maintained to  $180^\circ\text{C}$  for 24 h. Then the system was allowed to cool to room temperature naturally. The collected product was filtrated and washed with deionized water and absolute ethanol four times, then dried under vacuum at  $80^\circ\text{C}$ . 1-D  $\text{Ag}/\text{AgVO}_3$  nanoribbons were also constructed by the same method except 0.055 mol/L  $\text{AgNO}_3$  being added at the beginning.

### 2.3. Preparation of 2-D GO nanosheets

GO nanosheets were synthesized through the chemical exfoliation of graphite powder by using a modified Hummers' method [38]. Typically, 1 g of graphite powder was added to 23 mL of cooled (0 °C), concentrated H<sub>2</sub>SO<sub>4</sub>; then 3 g of KMnO<sub>4</sub> was added gradually under vigorous stirring. During this process, the temperature of the mixture was maintained below 20 °C using an ice bath. The mixture was further stirred at 35 °C for 30 min. Subsequently, 46 mL of ultrapure water was slowly added to the system, and the temperature of the system was increased to 98 °C. The mixture was maintained at that temperature for 15 min. The reaction was terminated by adding 140 mL of ultrapure Milli-Q water, which was followed by 10 mL of 30% H<sub>2</sub>O<sub>2</sub> solution. The solid product was separated by centrifugation and washed repeatedly with 5% HCl solution until sulfate could not be detected with BaCl<sub>2</sub>. Then the sample was dried in a vacuum oven at 25 °C overnight. To obtain GO nanosheets dispersed in water, 20 mg of thus-synthesized dried solid product was dispersed to 200 mL of ultrapure Milli-Q water at room temperature and exfoliated by ultrasonication for 8 h. At last, the final product was obtained by centrifugation, washed with deionized water, and dried in vacuum at 50 °C for 6 h.

### 2.4. Preparation of Ag/AgVO<sub>3</sub>/RGO ternary plasmonic photocatalyst

The Ag/AgVO<sub>3</sub>/RGO ternary plasmonic photocatalyst was synthesized through a facile one-step in-situ hydrothermal method. Briefly, 2-D GO nanosheets (80 mg) were added to ultrapure water (20 mL), and the suspension was sonicated for 3 h. Then, a solution of AgNO<sub>3</sub> (0.055 mol/L, 20 mL) was added to the suspension, which was stirred for 3 h to reach saturated adsorption of Ag<sup>+</sup> on the surface of GO. After that, NH<sub>4</sub>VO<sub>3</sub> (0.050 mol/L, 20 mL) was added to the suspension, which was stirred magnetically for 3 h. The resulted mixture was transferred into a Teflon-lined stainless-steel autoclave with a volume capacity of 100 mL. It was sealed and maintained to 180 °C for 24 h to simultaneously achieve crystallization of AgVO<sub>3</sub> and reduction of GO. Then the system was allowed to cool to room temperature naturally. The collected product was filtrated and washed with deionized water and absolute ethanol four times each, then dried under vacuum at 80 °C.

### 2.5. Preparation of AgVO<sub>3</sub>/RGO photocatalyst

The AgVO<sub>3</sub>/RGO was also synthesized by the above procedure except 0.050 mol/L of AgNO<sub>3</sub> solution being added.

### 2.6. Photoreaction procedures

The photocatalytic activities of as-synthesized photocatalysts were evaluated by decomposing Basic Fuchsin (BF) and Bisphenol A (BPA), respectively. Visible-light was generated by using 500 W Xe lamp irradiation with a 420 nm cut-off filter to remove light of  $\lambda < 420$  nm. For photodegradation of the BF (or BPA), 0.05 g of photocatalyst was put into 50 mL (20 mg/L) BF (or BPA) solutions. Prior to irradiation, the suspensions were magnetically stirred for 60 min to reach adsorption-desorption equilibrium in the dark. At given time intervals of visible-light irradiation, about 3 mL aliquots were collected from the reaction suspension, centrifuged at 8000 rpm for 10 min and filtered through a 0.22  $\mu$ m Millipore filter to remove the particles. The filtrate was subsequently analyzed by UV-vis spectroscopy at its maximum absorption wavelength. To ensure the reproducibility of the results, duplicate runs were performed for each condition for averaging the results.

The detection of the reactive species was investigated using similar procedures as described above for the photodegradation experiment. Benzoquinone (BQ), Ammonium Oxalate (AO) and

Isopropanol (IPA) were used as the scavengers of  $\bullet\text{O}_2^-$ ,  $\text{h}^+$  and  $\bullet\text{OH}$ , respectively. These scavengers were separately introduced into the reaction solution before the addition of the photocatalyst. In this study, the molar concentrations of the scavengers were added at a 100-fold relative to the initial molar concentration of BF or BPA.

### 2.7. Analytical methods

The degradation products of BPA were analyzed by Gas Chromatography–Mass Spectrometer (GC–MS). The analytical methods have been reported by our group [39]. Prior to GC–MS analysis; the samples were extracted with dichloromethane for three times. The extracted solution was dehydrated using anhydrous sodium sulfate and concentrated to 1 mL by rotary evaporation. After the solvent was blown away by the gentle nitrogen, trimethylsilylation was carried out at 50 °C for 30 min using 0.2 mL of bis(trimethylsilyl)trifluoroacetamide (BSTFA). The initial temperature of the column oven was 40 °C and following 1 min hold at this temperature, and then increased up to 300 °C with a heating rate of 6 °C/min. Helium was used as the carrier gas. Mass spectrometric detection was operated with 70 eV electron impact (EI) mode.

### 2.8. Characterization and calculation

X-ray diffraction (XRD) was performed at room temperature using an X'Pert-ProMPD (Holand) D/max- $\gamma$ A X-ray diffractometer. X-ray photo-electron spectroscopy (XPS) was used to identify surface chemical composition and chemical states of the catalysts on a PHI5000 Versa Probe electron spectrometer (ULVAC-PHI, Japan). The field emission scanning electron microscopy (FESEM) images were taken on a FEI-quanta 200F scanning electron microscope with an acceleration voltage of 20 kV. Transmission electron micrograph (TEM) and High resolution transmission electron microscopy (HRTEM) were taken on a FEI-Tecna F20 (200 kV) transmission electron microscope (FEI). Atomic force microscopy (AFM) study in the present work was performed by means of Veeco DI Nano-scope MultiMode V system. Fluorescence emission spectra were recorded on a FluoroMax 4 type fluorescence spectrophotometer with an excitation wavelength at 350 nm. The photocurrent experiments were measured using an electrochemical station (CHI660D, Shanghai Chenhua Ltd., China) in a conventional three-electrode configuration. The electrolyte was 0.01 M Na<sub>2</sub>SO<sub>4</sub> aqueous solution. UV-vis absorption spectra were performed using a Lambda 750 (PerkinElmer) spectrophotometer at a wavelength range of 200–800 nm. Raman spectra were recorded with a Labram-HR confocal laser Micro-Raman spectrometer equipped with an argon ion laser.

Three dimensional finite difference time domain (FDTD) simulations were performed to theoretically model near field distribution of the Ag/AgVO<sub>3</sub>/RGO. In the simulations, we assumed that the Ag nanoparticles were uniformly distributed in the x–y plane of the cross section of AgVO<sub>3</sub>/RGO nanoribbons and embedded in a background medium of water. Illumination of the Ag/AgVO<sub>3</sub>/RGO was simulated with a linearly polarized plane wave, propagating in the +Y direction.

## 3. Results and discussion

XRD was used to determine the phase structures of the as-prepared GO, RGO, AgVO<sub>3</sub>, Ag/AgVO<sub>3</sub> and Ag/AgVO<sub>3</sub>/RGO. As shown in Fig. 2a, the diffraction peak centered at about 10.8° can be attributed to the characteristic one of GO [40]. In the XRD pattern of RGO nanosheets, while the characteristic peak of GO disappears completely, confirming the effective reduction of GO to RGO nanosheets after the hydrothermal treatment and being in good



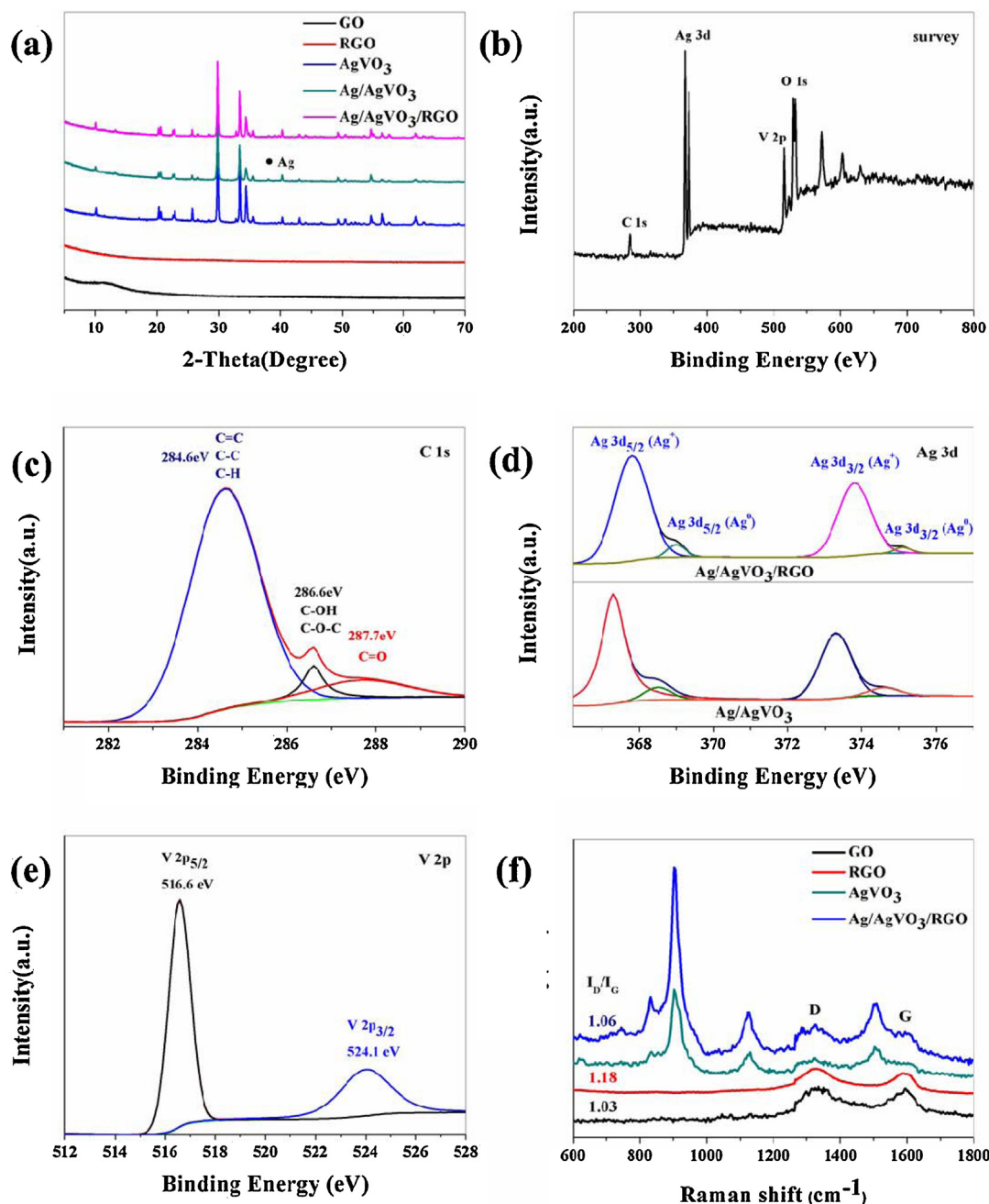


**Fig. 2.** (a) XRD patterns of the as-prepared samples ((●) mark shows the presence of Ag nanoparticles); (b) XPS spectra of the survey; (c) XPS spectra of C 1s; (d) XPS spectra of Ag 3d; (e) XPS spectra of V 2p; (f) Raman spectra of the as-prepared GO, RGO, AgVO<sub>3</sub> and Ag/AgVO<sub>3</sub>/RGO.

agreement with the previous reports [41]. As for the as-prepared AgVO<sub>3</sub>, the diffraction peaks can be readily indexed to the pure phase of  $\beta$ -AgVO<sub>3</sub> monoclinic structure [JCPDS: 29-11541]. The (501) peak is the strongest one, indicating the possible preferential orientation of the AgVO<sub>3</sub> nanoribbon [42]. For the Ag/AgVO<sub>3</sub> and Ag/AgVO<sub>3</sub>/RGO samples, apart from the diffraction peaks of  $\beta$ -AgVO<sub>3</sub> phase, the diffraction peak at angle 38.1° is found, which can be indexed to the face-centered cubic Ag (111) phase [JCPDS card: 04-0783]. No diffraction peak for the RGO or GO component could be observed in Ag/AgVO<sub>3</sub>/RGO due to its low percentage and the disappearance of characteristic peak after hydrothermal treatment.

GO can be reduced to RGO through a hydrothermal treatment because the overheated supercritical (SC) water can play the key role of reducing agent during the hydrothermal reaction [43].

Herein, the successful reduction of GO to RGO by hydrothermal process was verified by XPS and Raman spectra.

Fig. 2b represents a XPS survey spectrum of the Ag/AgVO<sub>3</sub>/RGO, suggesting that the sample contains C, Ag, V and O. Chemical binding energies are observed at 284.6, 368.1, 516.6 and 532.1 eV for C 1s, Ag 3d, V 2p, and O 1s, respectively. C 1s XPS spectrum (Fig. 2c) clearly shows three characteristic peaks, corresponding to nonoxygenated ring C bond (284.6 eV, including C–C, C=C, and C–H), the C–O in C–O–C or C–OH groups (286.6 eV), and the carbonyl C in C=O (287.7 eV), respectively [44]. Considering a hydrothermal deoxygenation/reduction process, the amount of oxygen-containing groups such as C–OH, C–O–C, and C=O should be lower than that of nonoxygenated C bonds such as C–C, C=C, and C–H. To illustrate the reduction degree of the GO nanosheets in the Ag/AgVO<sub>3</sub>/RGO, the peak area ratios of oxygen-containing C bonds

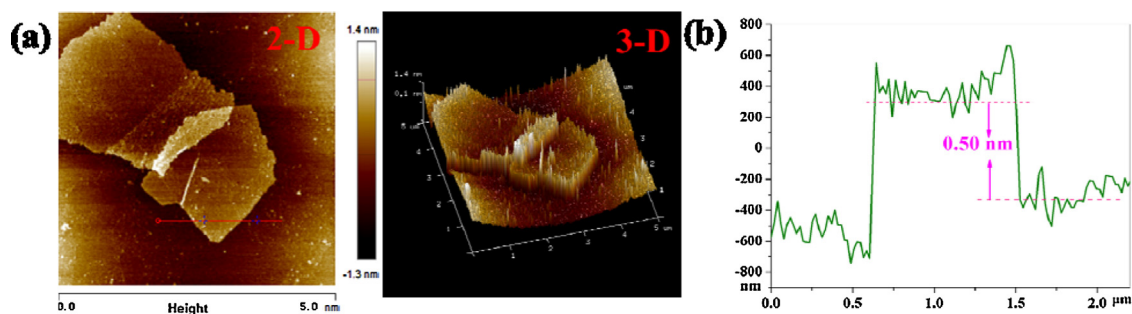


Fig. 3. AFM image of RGO ultrathin nanosheet.

to the total area are calculated to be 0.14 by the XPS C 1s peak area analysis. It is obvious that the content of oxygen-containing groups is pretty low, which provides a strong evidence for the reduction of GO in Ag/AgVO<sub>3</sub>/RGO. From the XPS spectra of the Ag species of the bare Ag/AgVO<sub>3</sub> (Fig. 2d), the two peaks at approximately 368.4 and 374.1 eV can be assigned to the binding energies of Ag 3d<sub>5/2</sub> and Ag 3d<sub>3/2</sub>, respectively. The two peaks can be further deconvoluted four bands (367.3, 368.5, 373.3, and 374.6 eV), implying the presence of different valences of silver species. The two strong peaks at 367.3 and 373.3 eV are attributed to Ag<sup>+</sup> 3d<sub>5/2</sub> and 3d<sub>3/2</sub>, respectively. And those relatively weak peaks at 368.5 and 374.6 eV are well matched with Ag<sup>0</sup> 3d<sub>5/2</sub> and 3d<sub>3/2</sub>, respectively. This result coincides with a previous study reported by Liang et al. [45]. Interestingly, compared with the bare Ag/AgVO<sub>3</sub>, the bands shift to higher binding energy in the Ag 3d XPS spectra of the Ag/AgVO<sub>3</sub>/RGO. This distinct shift suggests that the Ag/AgVO<sub>3</sub> of Ag/AgVO<sub>3</sub>/RGO works as an electron donor during the catalytic performance, leading to the facilitated charge separation and resulting in an improved catalytic performance of the Ag/AgVO<sub>3</sub>/RGO ternary

plasmonic photocatalyst [46]. In addition, the surface mole ratios of the metallic Ag<sup>0</sup> to the total Ag species for the as-preparation Ag/AgVO<sub>3</sub>, and Ag/AgVO<sub>3</sub>/RGO were semiquantitatively estimated to be ca. 0.09 and 0.05 by the XPS Ag 3d peak area analysis. These results verify the existence of metallic Ag<sup>0</sup> in our Ag/AgVO<sub>3</sub>/RGO ternary plasmonic photocatalyst, as suggested by the XRD spectra. Fig. 2e exhibited two peaks at 516.6 and 524.1 eV, which correspond to V 2p<sub>5/2</sub> and V 2p<sub>3/2</sub> of V<sup>5+</sup> in the AgVO<sub>3</sub>, respectively.

The reduction of GO during hydrothermal treatment was further confirmed by Raman spectra. As shown in Fig. 2f, two typical Raman bands at about 1335 and 1582 cm<sup>-1</sup>, which should be attributed to disordered sp<sup>2</sup> carbon (D-band) and well-ordered graphite (G-band), respectively [47,48]. Compared with the GO (1.03), the RGO shows a higher I<sub>D</sub>/I<sub>G</sub> intensity ratio (1.18), indicating that GO has been reduced into RGO after hydrothermal treatment [49]. The I<sub>D</sub>/I<sub>G</sub> intensity ratio in Ag/AgVO<sub>3</sub>/RGO (1.06) is lower than that in pure RGO (1.18). However, it is manifest that the Ag/AgVO<sub>3</sub>/RGO still shows a higher I<sub>D</sub>/I<sub>G</sub> intensity ratio than the GO, which confirms the formation of RGO in the Ag/AgVO<sub>3</sub>/RGO

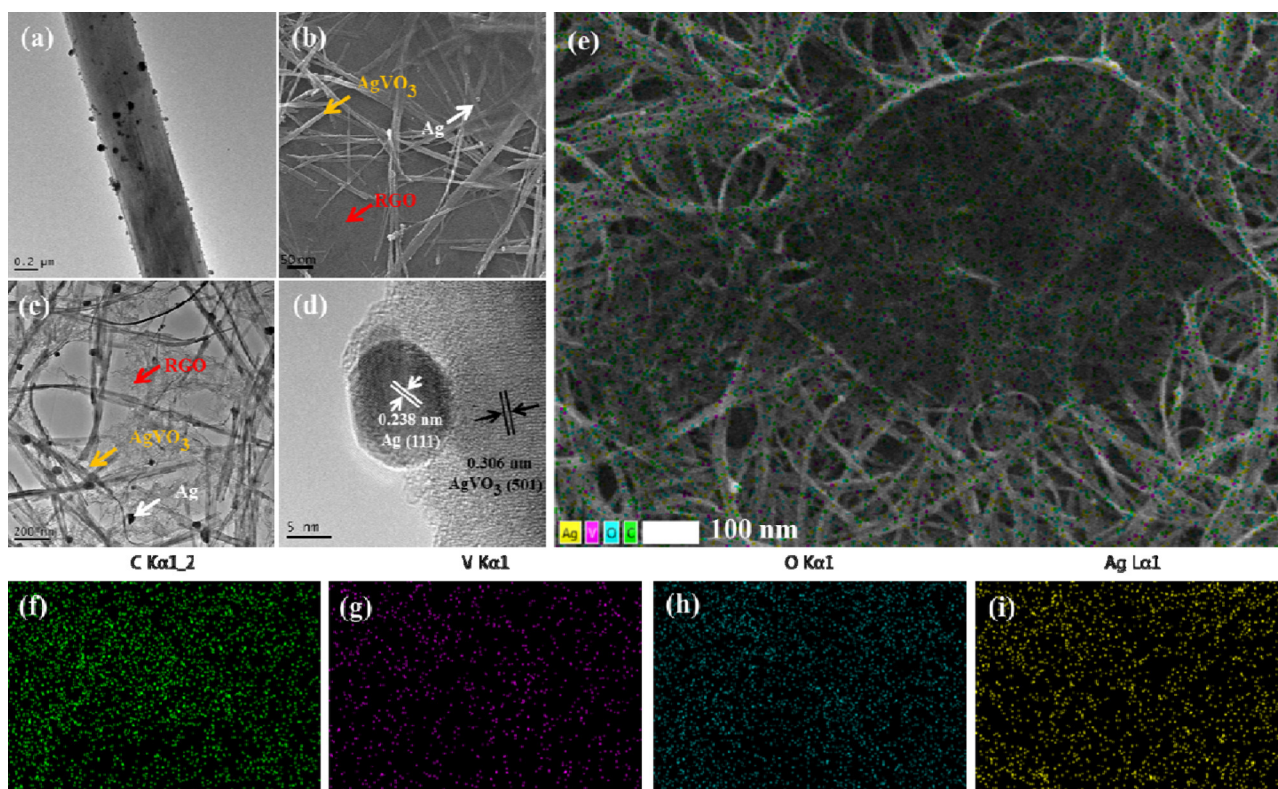
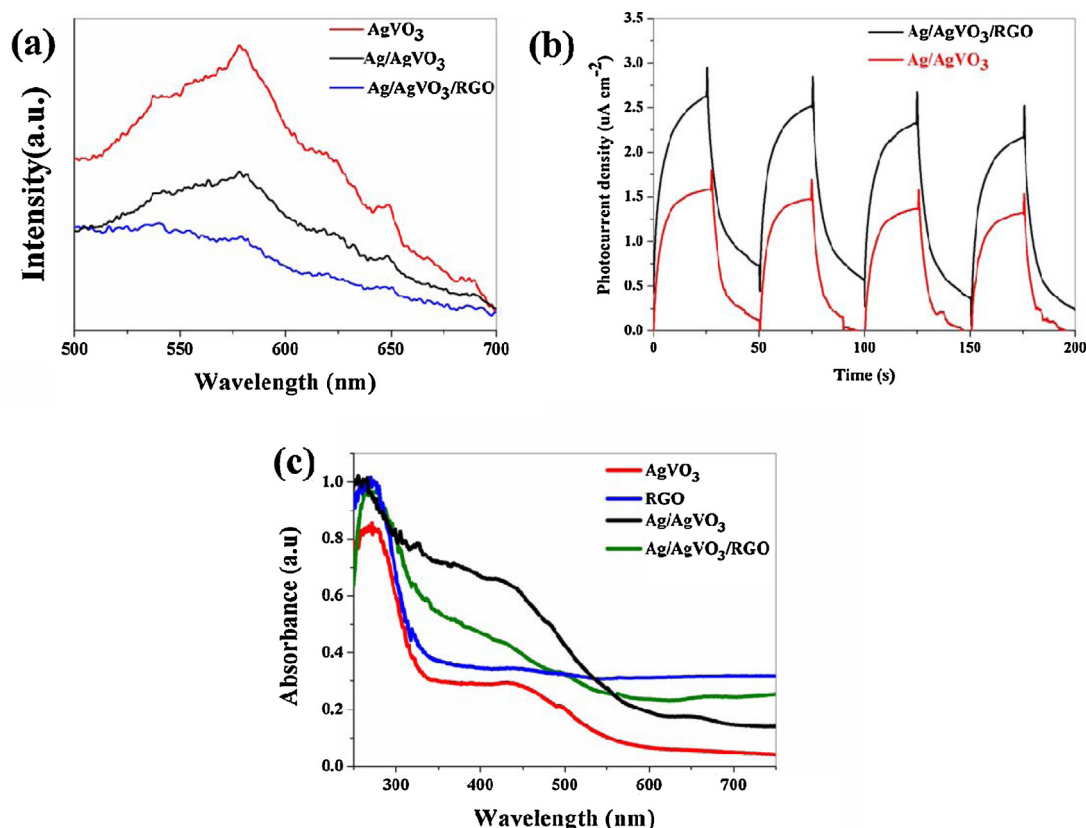


Fig. 4. (a) TEM image of Ag/AgVO<sub>3</sub>, (b) FESEM image of Ag/AgVO<sub>3</sub>/RGO, (c) TEM image of Ag/AgVO<sub>3</sub>/RGO, and (d) HRTEM image of Ag/AgVO<sub>3</sub>/RGO, (e) FESEM-EDS elemental mapping of Ag/AgVO<sub>3</sub>/RGO, the corresponding elemental mappings of (f) C, (g) V, (h) O, and (i) Ag elements.



**Fig. 5.** (a) Room-temperature fluorescence emission spectra of as-prepared AgVO<sub>3</sub>, Ag/AgVO<sub>3</sub> and Ag/AgVO<sub>3</sub>/RGO; (b) photo current of Ag/AgVO<sub>3</sub> and Ag/AgVO<sub>3</sub>/RGO under visible light irradiation; (c) UV-vis absorption spectra of AgVO<sub>3</sub>, RGO, Ag/AgVO<sub>3</sub>, and Ag/AgVO<sub>3</sub>/RGO.

ternary plasmonic photocatalyst during the hydrothermal treatment [50,51]. As for AgVO<sub>3</sub> sample, the strong peak at 886 cm<sup>-1</sup> may originate from either bridging O–V–O or V–O–Ag vibrations. The Raman peak at 808 cm<sup>-1</sup> can be associated with the stretching vibrations of the Ag–O–Ag bridges. The bridging V–O–V bond in the polymeric metavanadate chains is reflected by the 733 cm<sup>-1</sup> peak, corresponding to the asymmetric stretch. Fig. 2f also demonstrates that the peak intensities of Ag/AgVO<sub>3</sub>/RGO are significantly enhanced as compared with that of AgVO<sub>3</sub>, which is similar to the surface-enhanced Raman scattering (SERS) effect previously reported [52]. The strong Raman enhancement in the present system can be ascribed to SPR field induced by Ag nanoparticles in Ag/AgVO<sub>3</sub>/RGO. Therefore, it is revealed that the Ag nanoparticles formed on the surfaces of the AgVO<sub>3</sub> nanoribbons could greatly influence electronic structure in the plasmonic photocatalytic system.

To further understand the thickness of the RGO nanosheet, AFM measurement was carried out. Fig. 3a shows the 2-D and 3-D images of the RGO nanosheets. The thickness of RGO nanosheet is only 0.5 nm (Fig. 3b). This value of the thickness is as same as that of graphene reported at the first time [53].

The morphologies of the as-synthesized AgVO<sub>3</sub>, RGO, Ag/AgVO<sub>3</sub>, and Ag/AgVO<sub>3</sub>/RGO ternary plasmonic photocatalyst were investigated by FESEM and TEM. Fig. S1a and c shows the overall views of AgVO<sub>3</sub> and Ag/AgVO<sub>3</sub> nanoribbons, respectively. The FESEM images of the RGO (Fig. S1b) display a smooth surface with a wrinkled structure, which is a typical characteristic of nanosheet-like structure. From Fig. 4a, it can be seen that a single AgVO<sub>3</sub> nanoribbon with width of about 300 nm could be obtained when GO is not used. In contrast, when GO nanosheets are involved during the synthesis procedure; the widths of the obtained Ag/AgVO<sub>3</sub> nanoribbons are decreased to about 20–60 nm (Fig. 4b). Furthermore, the

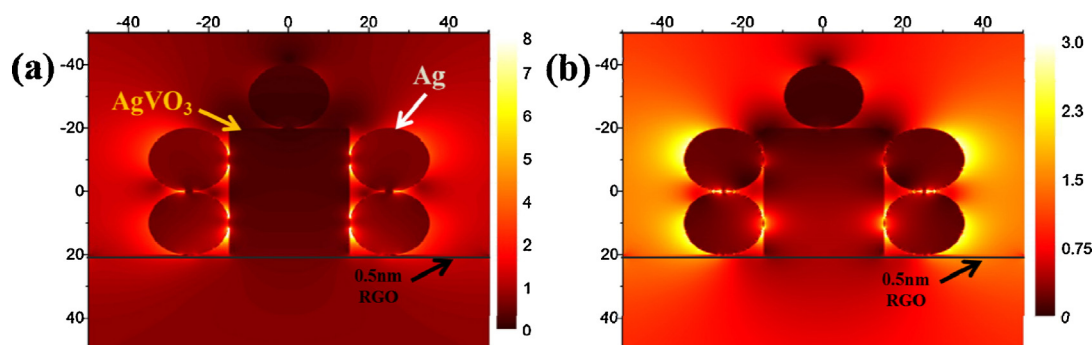


**Fig. 6.** Electric field distributions calculated at the cross-sections of Ag/AgVO<sub>3</sub>/RGO using the FDTD with light wavelengths of (a) 420 nm and (b) 620 nm. (The thickness and width of simulative AgVO<sub>3</sub> nanoribbon are 40 nm and 30 nm, respectively. The thickness of RGO nanosheets is 0.5 nm).



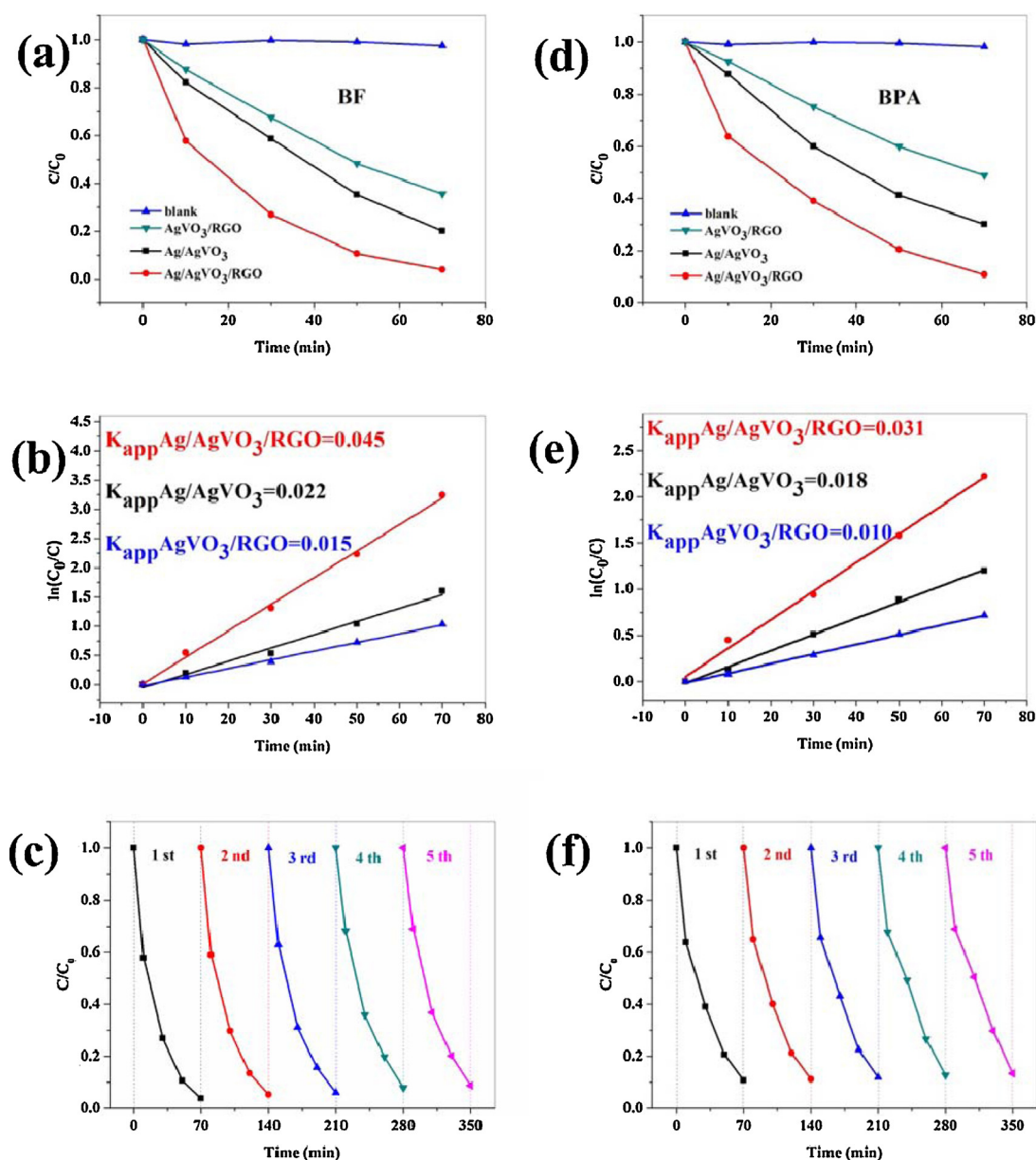


**Fig. 7.** (a) Photocatalytic activities and (b) pseudo-first-order kinetics of as-prepared photocatalysts for BF degradations, (c) five recycling runs of  $\text{Ag}/\text{AgVO}_3/\text{RGO}$  for BF degradations, (d) photocatalytic activities and (e) pseudo-first-order kinetics of as-prepared photocatalysts for BPA degradations, (f) five recycling runs of  $\text{Ag}/\text{AgVO}_3/\text{RGO}$  for BPA degradations.

detailed morphology and microstructure of the  $\text{Ag}/\text{AgVO}_3/\text{RGO}$  was examined by TEM and HRTEM. Fig. 4c clearly shows several 1-D  $\text{Ag}/\text{AgVO}_3$  nanoribbons with the widths of approximately 30 nm are attached on the 2-D gauze-like RGO nanosheets and the  $\text{Ag}/\text{AgVO}_3/\text{RGO}$  ternary plasmonic photocatalysts are formed. The 2-D RGO nanosheets serve as the supports to load  $\text{Ag}/\text{AgVO}_3$  nanoribbons in this ternary system. From the HRTEM image in Fig. 4d, the interplanar distances are determined to be 0.238 and 0.306 nm, which are in accordance with the d-spacing of the (1 1 1) crystal plane of Ag and (5 0 1) crystal plane of  $\text{AgVO}_3$ , respectively [54,55]. Based on the above characterization results, it could be confirmed that  $\text{Ag}/\text{AgVO}_3/\text{RGO}$  ternary plasmonic photocatalysts have been successfully prepared. Moreover, the interaction between the  $\text{Ag}/\text{AgVO}_3$  nanoribbons and the RGO nanosheets is so strong that ultrasonication during the sample preparation procedure for TEM analysis could not peel off these nanoribbons. Fig. 4e shows SEM-EDS elemental mapping of  $\text{Ag}/\text{AgVO}_3/\text{RGO}$ , EDS data collected

from all the points in the selected area display the existence of Ag, V, O and C elements. The 2D-projected elemental maps for four elements, disclosed in Fig. 4f–i, demonstrates the distribution of these elements throughout the  $\text{Ag}/\text{AgVO}_3/\text{RGO}$  sample.

The fluorescence emission spectra of the samples were analyzed to evaluate the separation rate of electron–hole pairs, which could greatly affect the catalytic activity (Fig. 5a). The main emission peak is centered at about 580 nm for the pure  $\text{AgVO}_3$  sample, which can be ascribed to the band gap recombination of electron–hole pairs. The emission spectrum of  $\text{AgVO}_3$  has the greatest relative intensity, indicating that electrons and holes of  $\text{AgVO}_3$  are easy to recombine. The relative intensity of  $\text{Ag}/\text{AgVO}_3$  is lower than that of  $\text{AgVO}_3$ , indicating that the Ag nanoparticles formed could partially suppress the recombination of electrons and holes. The suppression could be attributed to the Schottky barrier formed at the Ag– $\text{AgVO}_3$  interface which could act as an electron store to prevent electron–hole recombination efficiently [56]. As expected,

once Ag/AgVO<sub>3</sub> was hybridized with RGO further, Ag/AgVO<sub>3</sub>/RGO showed the lowest fluorescence emission intensity corresponding to the lowest recombination rate of electron–hole pairs. This could result from the electron transfer in the Ag/AgVO<sub>3</sub> and the further interfacial transfer in the RGO due to the excellent electronic conductivity and the high charge carrier mobility of the RGO [57]. Photocurrent measurements were also carried out to evaluate the capacity of photogenerated charge separation. The higher photocurrent value means more efficient separation of photogenerated electron–hole pairs. As shown in Fig. 5b, compared with Ag/AgVO<sub>3</sub>, the Ag/AgVO<sub>3</sub>/RGO displayed a much enhanced photocurrent density.

UV–vis absorption spectra of RGO, AgVO<sub>3</sub>, Ag/AgVO<sub>3</sub> and Ag/AgVO<sub>3</sub>/RGO are illustrated in Fig. 5c. The bare RGO sample displays strong absorption both in the ultraviolet and visible regions. For the pure AgVO<sub>3</sub>, its absorbance edge is at around 590 nm, and the band-gap energy is approximate 2.1 eV. Compared with AgVO<sub>3</sub>, Ag/AgVO<sub>3</sub> and Ag/AgVO<sub>3</sub>/RGO samples exhibit broad absorption in the whole visible region and the absorption intensities increase, which should be attributed to the SPR effect of the Ag nanoparticles formed on the surfaces of the AgVO<sub>3</sub> nanoribbons. Obviously, the Ag nanoparticles could remarkably enhance the absorption of light. Therefore, the formation rate of electron–hole pairs on the photocatalyst surface/interfaces also increases substantially, resulting in the better catalytic performance.

To explore the SPR and the electric field enhancement caused by the Ag nanoparticles, the electric field distribution was simulated using the FDTD method. In the simulations, in order to simplify the calculation, the model showed in Fig. 6 is the cross sectional view of an Ag/AgVO<sub>3</sub>/RGO. The cross section was formed by cutting perpendicularly to the length of the nanoribbon. The importance of the intense local fields can be seen in Fig. 6, illustrating a cross-sectional plot of the electric field distribution of the hot spot regions in the *y*-dimension. The local “hot spots” can be seen in regions among nearly touching Ag nanoparticles. This is a well-known phenomenon, corroborated by the calculations of Cronin research group [58]. In the local hot spot region, the electric field intensity at the AgVO<sub>3</sub> surface is much higher than that of the incident electromagnetic radiation under 420 nm wavelength illuminations owing to SPR of the Ag nanoparticles (Fig. 6a). This process should result in the rapid formation of electron–hole pairs near the surface of AgVO<sub>3</sub>. Simulation results shown in Fig. 6b also clearly demonstrates the occurrence of intense electric fields at the nearby AgVO<sub>3</sub> surface under 620 nm wavelength illuminations due to SPR of the Ag nanoparticles. These could evidently explain the reason why the samples display excellent photoactivity in the visible-light region ( $\lambda > 420$  nm).

The photocatalytic activities of Ag/AgVO<sub>3</sub>, AgVO<sub>3</sub>/RGO and Ag/AgVO<sub>3</sub>/RGO were evaluated in terms of the photodegradation of BF under visible light irradiation. A dark adsorption experiment was performed for 60 min prior to the visible-light irradiation to achieve an equilibrium adsorption state; the Ag/AgVO<sub>3</sub>/RGO displayed distinctly higher adsorptive ability for BF molecules than the bare Ag/AgVO<sub>3</sub> (Fig. S2 dark adsorption curves). This could be

ascribed to the hybridization of RGO species in the former system, which could facilitate the adsorption of pollutant molecules due to the non-covalent intermolecular  $\pi$ – $\pi$  interactions between the pollutant molecules and RGO nanosheets [59]. Fig. 7a demonstrates the time profiles of BF photodegradation over the samples (The blank experiment showed that there was no obvious photodegradation of BF in the absence of photocatalyst). It reveals that BF is gradually decomposed with the increase of visible light irradiation time. After 70 min of visible-light irradiation, 79.9% of BF removal was achieved over Ag/AgVO<sub>3</sub>, while the Ag/AgVO<sub>3</sub>/RGO displayed a relatively high photocatalytic activity with BF degradation of 96.1%. It is clear that Ag/AgVO<sub>3</sub>/RGO exhibits the highest photocatalytic activity among these samples. The photocatalytic degradation of BF is a pseudo-first-order reaction and its kinetics can be expressed as  $\ln(C_0/C) = k_{app} t$  [60], where *C* is the concentration of the BF at time *t*, *C*<sub>0</sub> is the initial concentration of the BF solution, and the slope *k* is the apparent reaction rate constant. As shown in Fig. 7b, the Ag/AgVO<sub>3</sub>/RGO reveals the highest value with *k*<sub>app</sub> of 0.045 min<sup>−1</sup>, which is found to be about 2 and 3 times higher than that of Ag/AgVO<sub>3</sub> (0.022 min<sup>−1</sup>) and AgVO<sub>3</sub>/RGO (0.015 min<sup>−1</sup>). The lifetime of the catalyst is a significant parameter for the catalytic process. The stability and the reusability of the Ag/AgVO<sub>3</sub>/RGO ternary plasmonic photocatalyst during BF degradation were investigated. The photocatalytic processes were repeated five times. As shown in Fig. 7c, the photocatalyst exhibits adequate stability. At the first cycling run, the photocatalytic degradation is 96.1%; after the fifth cycling run, the photocatalytic degradation is 91.2%, without remarkable reduction.

The photocatalytic performances of samples were also evaluated by the degradation of BPA solution, a colorless transparent solution, under visible light irradiation, as shown in Fig. 7d–f. The results are similar to BF degradations; Ag/AgVO<sub>3</sub>/RGO exhibits the highest *k* value of 0.031 min<sup>−1</sup>. The stability of the Ag/AgVO<sub>3</sub>/RGO during BPA degradation was also investigated, as shown in Fig. 7f, the sample exhibited adequate stability.

As shown in Fig. 8, the excellent stability of the catalyst could be further confirmed by TEM, XRD, and XPS of the samples measured after the recycling experiments, where negligible changes are observed after the photocatalytic performance. In order to study the changes of RGO and the content of Ag<sup>0</sup> in Ag/AgVO<sub>3</sub>/RGO before and after the photodegradation reaction, C 1s and Ag 3d peak area analysis of the used sample are shown in Tables 1 and 2, respectively. Decrease of the ratio oxygen-containing C bonds to the total area in Ag/AgVO<sub>3</sub>/RGO after use indicates further reduction of RGO in the sample during photocatalytic experiment (please see Table 1). This phenomenon is consistent with the literature report [51]. As shown in Table 2, the surface Ag<sup>0</sup> content of Ag/AgVO<sub>3</sub> after the photocatalytic performance is 0.16, which displays negligible changes compared with that before the photodegradation experiment. Compared with the Ag/AgVO<sub>3</sub> sample, Ag/AgVO<sub>3</sub>/RGO shows small increase of Ag<sup>0</sup> content (0.08). These experimental results exhibit that the introducing of RGO effectively improves the charger separation and transfer efficiency of the Ag/AgVO<sub>3</sub>/RGO sample.

**Table 1**  
XPS C 1s peak area analysis of sample before and after the photodegradation reaction.

Photocatalyst	Peak position (eV)	Peak area	Peak attribution	Surface oxygen-containing C bonds to the total area
Ag/AgVO <sub>3</sub> /RGO (before)	284.600	575.392	C=C, C–C, C–H	0.14
	286.600	38.018	C–OH, C–O–C	
	287.700	60.423	C=O	
Ag/AgVO <sub>3</sub> /RGO (after)	284.600	646.460	C=C, C–C, C–H	0.12
	286.600	32.439	C–OH, C–O–C	
	287.700	52.810	C=O	



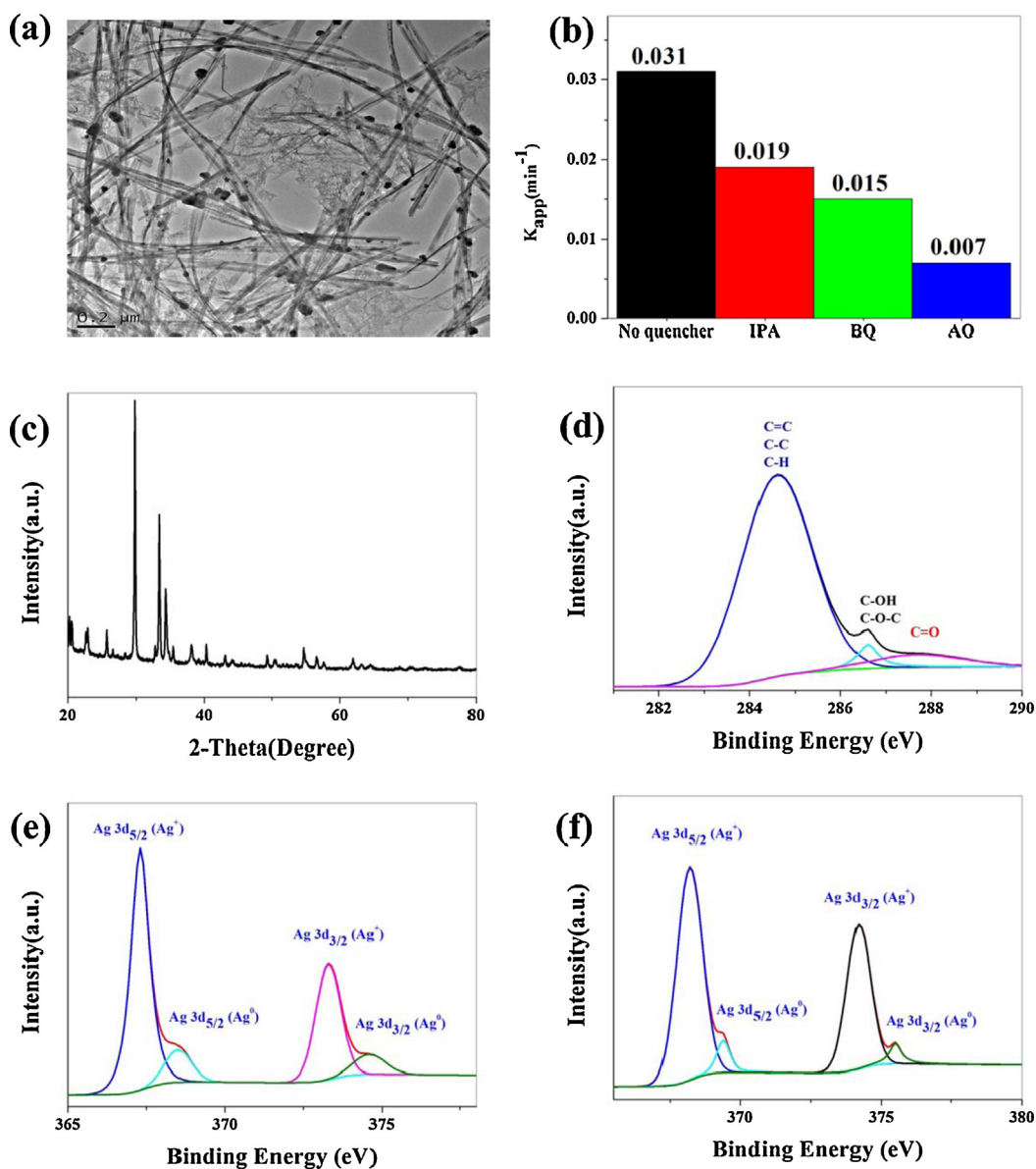


**Fig. 8.** (a) TEM image of Ag/AgVO<sub>3</sub>/RGO after the photocatalytic reaction, (b)  $k_{app}$  values of Ag/AgVO<sub>3</sub>/RGO with selected quenchers, (c) XRD pattern of Ag/AgVO<sub>3</sub>/RGO, (d) XPS spectra of C 1s of Ag/AgVO<sub>3</sub>/RGO, (e) XPS spectra of Ag 3d of Ag/AgVO<sub>3</sub> and (f) XPS spectra of Ag 3d of Ag/AgVO<sub>3</sub>/RGO after the photocatalytic reaction.

**Table 2**

XPS Ag 3d peak area analysis of sample before and after the photodegradation reaction.

Photocatalyst	Peak position (eV)	Peak area	Peak attribution	Surface Ag <sup>0</sup> content (Ag <sup>0</sup> to the total Ag species)
Ag/AgVO <sub>3</sub> (before)	367.300	4237.793	Ag <sup>+</sup>	0.09
	368.500	402.515	Ag <sup>0</sup>	
	373.300	2416.733	Ag <sup>+</sup>	
	374.600	286.574	Ag <sup>0</sup>	
Ag/AgVO <sub>3</sub> (after)	367.300	3622.766	Ag <sup>+</sup>	0.16
	368.500	613.875	Ag <sup>0</sup>	
	373.300	2118.965	Ag <sup>+</sup>	
	374.600	456.913	Ag <sup>0</sup>	
Ag/AgVO <sub>3</sub> /RGO (before)	368.200	4312.551	Ag <sup>+</sup>	0.05
	369.400	260.843	Ag <sup>0</sup>	
	374.200	2806.363	Ag <sup>+</sup>	
	374.500	109.217	Ag <sup>0</sup>	
Ag/AgVO <sub>3</sub> /RGO (after)	368.200	4016.112	Ag <sup>+</sup>	0.08
	369.400	381.790	Ag <sup>0</sup>	
	374.200	2509.658	Ag <sup>+</sup>	
	374.500	263.544	Ag <sup>0</sup>	

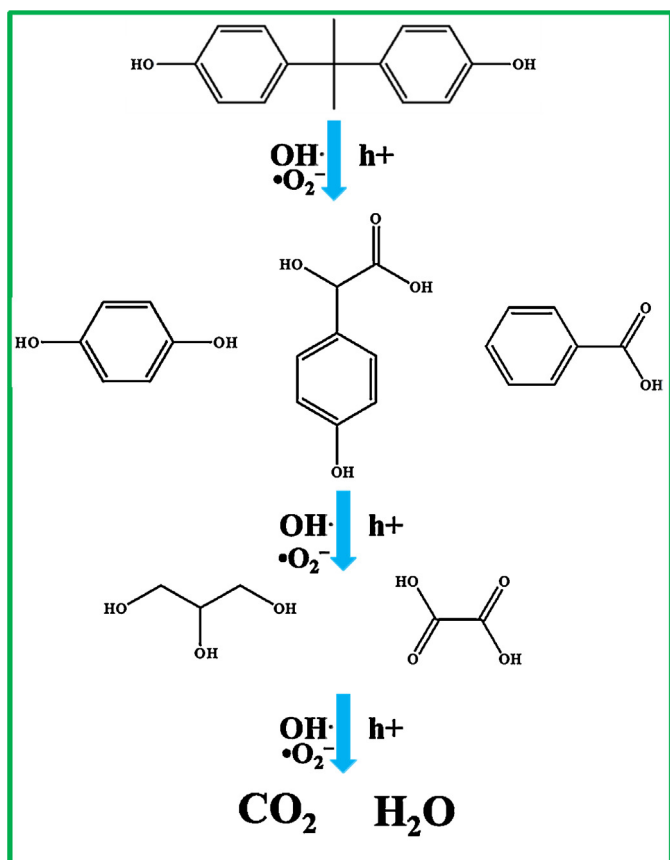


Fig. 9. Proposed BPA degradation pathway on the Ag/AgVO<sub>3</sub>/RGO.

It is generally acknowledged that the dyes and organic pollutants can be photodegraded via photocatalytic oxidation process. There are a lot of main reactive oxygen species involved in the photocatalytic oxidation process, such as •O<sub>2</sub><sup>-</sup>, h<sup>+</sup> and •OH [61–63]. In order to detect the effect of these reactive species on the degradation of BPA, as an •O<sub>2</sub><sup>-</sup> scavenger, benzoquinone was added to the reaction system, and ammonium oxalate was introduced as the scavenger of h<sup>+</sup>. Isopropanol was adopted to quench •OH. The comparative experiment with no quencher was also carried out under otherwise identical conditions. As a result of quenching, photocatalytic oxidation reaction will be partly suppressed and *k*<sub>app</sub> is lowered. The more *k*<sub>app</sub> is lowered by scavengers, the more important role the corresponding oxidizing species plays in the reaction. From Fig. 8b, upon the addition of ammonium oxalate, the *k*<sub>app</sub> decreased seriously, suggesting that h<sup>+</sup> is the main reactive species in the photocatalytic process.

The intermediates and products formed in the photocatalytic degradation of BPA were identified by the analysis of mass spectra obtained from GC–MS applications and by the comparison with the library data of NIST. Five products were identified by the mass fragment peak. Table 3 lists main fragments (*m/z*) and retention time (min) obtained for five intermediate products. In the primary photocatalytic degradation of BPA, the attack of reactive species such as h<sup>+</sup>, •O<sub>2</sub><sup>-</sup> and •OH produce hydroquinone, 4-hydroxyphenylglycolic acid, and benzoic acid. These single aromatic intermediates are presumably further oxidized through ring-rupturing reactions into aliphatic compounds containing oxalic acid and glycerol. Finally, the mineralization reaction to carbon dioxide may occur since the stoichiometric formation of CO<sub>2</sub> was observed in the present study. Thus, in this work, it was proposed that the photocatalytic degradation pathway of BPA in water with Ag/AgVO<sub>3</sub>/RGO, as illustrated in Fig. 9.

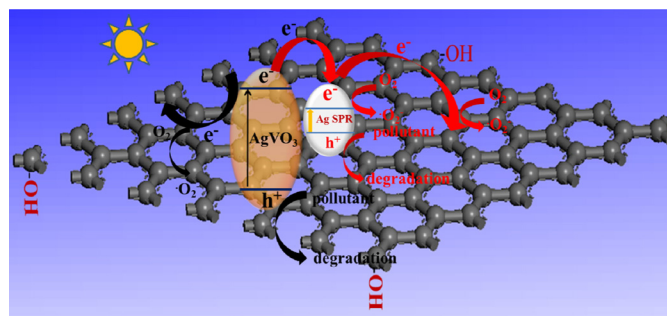
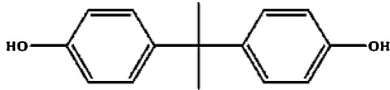
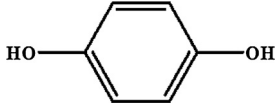
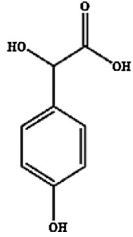
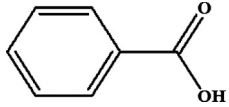
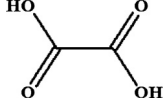
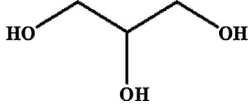


Fig. 10. Proposed mechanism of photocatalytic reaction over Ag/AgVO<sub>3</sub>/RGO system.

On basis of the above-described experimental results, the mechanism of photocatalytic degradation of organic pollutants over the Ag/AgVO<sub>3</sub>/RGO ternary plasmonic photocatalyst under visible light irradiation is proposed, as illustrated in Fig. 10. The electrons and holes can be produced from AgVO<sub>3</sub> under the visible-light irradiation. In addition, Ag nanoparticles are also excited due to the localized SPR and generate electron–hole pairs [64,65]. The excited electrons in the conduction band of AgVO<sub>3</sub> can transfer quickly toward Ag nanoparticles due to the excellent conductivity and the storing electrons capacity of the Ag nanoparticles. Similar suggestions were proposed on Ag<sub>2</sub>O [66] and Ag<sub>3</sub>PO<sub>4</sub> [67] photocatalysts. Meanwhile, the electrons in the conduction band of AgVO<sub>3</sub> may be also transferred to the surface of RGO, which can facilitate the fast and long-range interfacial charge transfer along the  $\pi$ – $\pi$  graphitic carbon network owing to RGO with high conductivity. Additionally, it is possible that the electrons generated from Ag nanoparticles could also be transferred to RGO [68]. Clearly, both the AgVO<sub>3</sub> and plasmon-excited Ag nanoparticles serve as electron transfer media in the vectorial electron transfers of AgVO<sub>3</sub> → RGO and/or AgVO<sub>3</sub> → Ag → RGO, thus reducing the recombination possibility with photo generated holes. Moreover, the excess electrons can be away from AgVO<sub>3</sub> as far as possible, instead of reduction of silver ions in the AgVO<sub>3</sub>, which ensures the stability of the photocatalyst. The electrons in the plasmon-excited Ag nanoparticles and on the surface of RGO could be trapped by O<sub>2</sub> to form •O<sub>2</sub><sup>-</sup> reactive oxygen species, followed by the generation of •OH [69]. The photogenerated holes on AgVO<sub>3</sub> and Ag could then oxidize the organic molecule directly. The reactive species including •O<sub>2</sub><sup>-</sup>, •OH, and h<sup>+</sup> have the potential for the degradation of BF and BPA, and the control experiments using scavengers reveal h<sup>+</sup> is the main reactive species in this photocatalytic process.

From the aforementioned, we could propose an explanation for the enhanced photocatalytic performance observed from the Ag/AgVO<sub>3</sub>/RGO ternary plasmonic photocatalyst. Firstly, Ag nanoparticles play the important role on the property of the photocatalyst. The strong SPR absorption of Ag nanoparticles will remarkably enhance the absorbance of the samples in the visible light region. Therefore, the formation rate of electron–hole pairs on the sample increases substantially, resulting in better catalytic performance. In addition, the hybridization of RGO species in Ag/AgVO<sub>3</sub>/RGO not only facilitates the adsorption of pollutant molecules due to the non-covalent intermolecular  $\pi$ – $\pi$  interactions between the pollutant molecules and RGO nanosheets, but also promotes the fast and long-range interfacial charge transfer along the  $\pi$ – $\pi$  graphitic carbon network owing to RGO with high conductivity. Lastly, the widths of Ag/AgVO<sub>3</sub> nanoribbons in the case of Ag/AgVO<sub>3</sub>/RGO are smaller than that of bare Ag/AgVO<sub>3</sub> nanoribbons, which may also contribute partially to the enhanced photocatalytic performance. Moreover, as suggested by our XPS spectra, the 1-D Ag/AgVO<sub>3</sub> nanoribbons and 2-D RGO nanosheets may serve as electron donor and electron acceptor,

**Table 3**  
Identification of the intermediates of BPA by GC–MS.

Product	Retention (time/min)	<i>m/z</i>	Name	Molecular structure
A	10.77	228	Bisphenol A	
B	18.69	110	Hydroquinone	
C	35.87	168	4-Hydroxyphenylglycolic acid	
D	15.34	122	Benzoic acid	
E	20.24	90	Oxalic acid	
F	15.9	92	Glycerol	

respectively, in the Ag/AgVO<sub>3</sub>/RGO ternary plasmonic photocatalyst. Thus, the electrons originally photogenerated on the 1D Ag/AgVO<sub>3</sub> nanoribbons can migrate into 2-D RGO nanosheets through a percolation process [70] during the photocatalytic reaction.

As discussed above, the hybridizations of 1-D Ag/AgVO<sub>3</sub> nanoribbons with 2-D RGO nanosheets could result in the enhanced absorbance in the visible light region, the nice adsorptive capacity to BF molecules, the smaller widths of the Ag/AgVO<sub>3</sub> nanoribbons, the facilitated charge transfer, and the suppressed recombination of electron–hole pairs in Ag/AgVO<sub>3</sub>/RGO ternary plasmonic photocatalyst. These multi-factors would be attributed to the enhanced catalytic performance observed from Ag/AgVO<sub>3</sub>/RGO ternary plasmonic photocatalyst.

#### 4. Conclusions

We developed a facile one-step in-situ hydrothermal method to synthesize Ag/AgVO<sub>3</sub>/RGO ternary plasmonic photocatalyst. In this innovative hybrid structure, 1-D Ag/AgVO<sub>3</sub> nanoribbons are uniformly dispersed on 2-D RGO nanosheet surfaces. The as-obtained Ag/AgVO<sub>3</sub>/RGO exhibits excellent light-trapping ability and photocatalytic performance, which could be attributed to the enhanced absorbance in the visible light region, the nice adsorptive capacity to pollutant molecules, the smaller widths of the Ag/AgVO<sub>3</sub> nanoribbons, the facilitated charge transfer, and the suppressed recombination of electron–hole pairs in Ag/AgVO<sub>3</sub>/RGO. The present study will benefit the development of the new plasmonic photocatalysts and would be of great importance to meet the environmental demands in the future.

#### Acknowledgements

The authors greatly acknowledge the National Natural Science Foundation of China (No. 21177055 and 51278242), the Natural Science Foundation of Jiangsu Province (BK2012732), the sixteenth batch of the Science and Technology Development Plan of Suzhou city (ZXG201441), the Jiangsu Province Graduate Student Scientific Research Innovation Project (KYLX0050), and the China Postdoctoral Science Foundation funded the 54th batches surface (2013M541646).

The authors thank Dr. Li H. (Department of Plant, Soil and Microbial Sciences, Michigan State University) for his great help at language modification and composition suggestion, and Dr. Shi X. B. (Institute of Functional Nano and Soft Materials (FUNSOM) and Collaborative Innovation Center of Suzhou Nano Science and Technology, Soochow University), Dr. Yuan L. (State Key Laboratory of Inorganic Synthesis and Preparative Chemistry, College of Chemistry, Jilin University) and Dr. Wu H. W. (National Laboratory of Solid State Microstructures and Department of Physics, Nanjing University) for their helps in discussing the experimental results.

#### Appendix A. Supplementary data

Supplementary data associated with this article can be found, in the online version, at <http://dx.doi.org/10.1016/j.apcatb.2015.05.002>.

#### References



- [1] M.A. Shannon, P.W. Bohn, M. Elimelech, J.G. Georgiadis, B.J. Marinas, A.M. Mayes, *Nature* 452 (2008) 301–310.
- [2] C. Feng, G. Li, P. Ren, Y. Wang, X. Huang, D. Liang, *Appl. Catal. B* 158 (2014) 224–232.
- [3] G. Liu, Y.N. Zhao, C.H. Sun, F. Li, G.Q. Lu, H.M. Cheng, *Angew. Chem. Int. Ed.* 120 (2008) 4592–4596.
- [4] H. Shi, G. Li, H. Sun, T. An, H. Zhao, P.-K. Wong, *Appl. Catal. B* 158 (2014) 301–307.
- [5] M. Zhang, C.C. Chen, W.H. Ma, J.C. Zhao, *Angew. Chem. Int. Ed.* 47 (2008) 9730–9733.
- [6] T. Liu, B. Li, Y. Hao, F. Han, L. Zhang, L. Hu, *Appl. Catal. B* 165 (2015) 378–388.
- [7] C. Cui, Y. Wang, D. Liang, W. Cui, H. Hu, B. Lu, S. Xu, X. Li, C. Wang, Y. Yang, *Appl. Catal. B* 158 (2014) 150–160.
- [8] G. Schubert, A. Gazsi, F. Solymosi, *J. Catal.* 313 (2014) 127–134.
- [9] Z.G. Zou, J.H. Ye, K. Sayama, H. Arakawa, *Nature* 414 (2001) 625–627.
- [10] H.-M. Chiu, T.-H. Yang, Y.-C. Hsueh, T.-P. Peng, J.-M. Wu, *Appl. Catal. B* 163 (2015) 156–166.
- [11] X. Bai, R. Zong, C. Li, D. Liu, Y. Liu, Y. Zhu, *Appl. Catal. B* 147 (2014) 82–91.
- [12] Z.J. Chen, S.K. Gao, R.H. Li, M.D. Wei, K.M. Wei, H.S. Zhou, *Electrochim. Acta* 53 (2008) 8134–8137.
- [13] L.Q. Mai, L. Xu, Q. Gao, C.H. Han, B. Hu, Y.Q. Pi, *Nano Lett.* 10 (2010) 2604–2608.
- [14] H. Xu, H.M. Li, L. Xu, C.D. Wu, G.S. Sun, Y.G. Xu, J.Y. Chu, *Ind. Eng. Chem. Res.* 48 (2009) 10771–10778.
- [15] L.C. Chen, G.T. Pan, T.C.K. Yang, T.W. Chung, C.M. Huang, *J. Hazard. Mater.* 178 (2010) 644–651.
- [16] J. Ren, W.Z. Wang, M. Shang, S.M. Sun, L. Zhang, J. Chang, *J. Hazard. Mater.* 183 (2010) 950–953.
- [17] H.F. Shi, Z.S. Li, J.H. Kou, J.H. Ye, Z.G. Zou, *J. Phys. Chem. C* 115 (2011) 145–151.
- [18] W. Zhao, Y. Guo, Y. Faiz, W. Yuan, C. Sun, S. Wang, Y. Deng, Y. Zhuang, Y. Li, X. Wang, H. He, S. Yang, *Appl. Catal. B* 163 (2015) 288–297.
- [19] W. Zhao, Y. Guo, S. Wang, H. He, C. Sun, S. Yang, *Appl. Catal. B* 165 (2015) 335–343.
- [20] P. Ju, H. Fan, B.L. Zhang, K. Shang, T. Liu, S.Y. Ai, D. Zhang, *Sep. Purif. Technol.* 109 (2013) 107–110.
- [21] S.Y. Zhang, W.Y. Li, C.S. Li, J. Chen, *J. Phys. Chem. B* 110 (2006) 24855–24863.
- [22] S.J. Bao, Q.L. Bao, C.M. Li, T.P. Chen, C.Q. Sun, Z.L. Dong, Y. Gan, J. Zhang, *Small* 3 (2007) 1174–1177.
- [23] J.M. Song, Y.Z. Lin, H.B. Yao, F.J. Fan, X.G. Li, S.H. Yu, *ACS Nano* 3 (2009) 653–660.
- [24] P. Wang, B.B. Huang, X.Y. Qin, X.Y. Zhang, Y. Dai, J.Y. Wei, M.H. Whangbo, *Angew. Chem. Int. Ed.* 41 (2008) 7931–7933.
- [25] Y.P. Bi, H. Hu, S.X. Ouyang, Z. Jiao, G.X. Lu, J.H. Ye, *J. Mater. Chem.* 22 (2012) 14847–14850.
- [26] K. Mori, M. Kawashima, M. Che, H. Yamashita, *Angew. Chem.* 122 (2010) 8780–8783.
- [27] D.J. Wang, G.L. Xue, Y.Z. Zhen, F. Fu, D.S. Li, *J. Mater. Chem.* 22 (2012) 4751–4758.
- [28] W.H. Hung, M. Aykol, D. Valley, W. Hou, S.B. Cronin, *Nano Lett.* 10 (2010) 1314–1318.
- [29] X. Zhang, Y. Liu, S.T. Lee, S. Yang, Z.H. Kang, *Energy Environ. Sci.* 7 (2014) 1409–1419.
- [30] J.L. Long, H.J. Chang, Q. Gu, J. Xu, L.Z. Fan, S.C. Wang, Y.G. Zhou, W. Wei, L. Huang, X.X. Wang, P. Liu, W. Huang, *Energy Environ. Sci.* 7 (2014) 973–977.
- [31] P. Wang, B.B. Huang, Q. Zhang, X. Zhang, X. Qin, Y. Dai, J. Zhan, J. Yu, H. Liu, Z. Lou, *Chem. – Eur. J.* 16 (2010) 10042–10047.
- [32] Y.G. Lin, Y.K. Hsu, Y.C. Chen, S.B. Wang, J.T. Miller, L.C. Chen, K.H. Chen, *Energy Environ. Sci.* 5 (2012) 8917–8922.
- [33] Z.X. Ji, M.N. Ismail, D.M. Callahan Jr., E. Pandowo, Z.H. Cai, T.L. Goodrich, K.S. Ziemer, J. Warzywoda, A. Sacco Jr., *Appl. Catal. B* 102 (2011) 323–333.
- [34] M.S. Zhu, P.L. Chen, M.H. Liu, *Langmuir* 28 (2012) 3385–3390.
- [35] B. Luo, S. Liu, L. Zhi, *Small* 8 (2010) 630–646.
- [36] B.J. Jiang, Y.H. Wang, J.Q. Wang, C.G. Tian, W.J. Li, Q.M. Feng, Q.J. Pan, H.G. Fu, *ChemCatChem* 5 (2013) 1359–1367.
- [37] M.S. Zhu, P.L. Chen, M.H. Liu, *ACS Nano* 5 (2011) 4529–4536.
- [38] C. Nethravathi, M. Rajamathi, *Carbon* 46 (2008) 1994–1998.
- [39] S. Luo, S. Yang, C. Sun, X. Wang, *Water Res.* 45 (2011) 1519–1528.
- [40] S.D. Perera, R.G. Mariano, K. Vu, N. Nour, O. Seitz, Y. Chabal, K.J. Balkus Jr., *ACS Catal.* 2 (2012) 949–956.
- [41] P. Wang, J. Wang, X.F. Wang, H.G. Yu, J.G. Yu, M. Lei, Y.G. Wang, *Appl. Catal. B* 132 (2013) 452–459.
- [42] M.R. Parida, C. Vijayan, C.S. Rout, C.S.S. Sandeep, R. Philip, *Appl. Phys. Lett.* 100 (2012) 121119.
- [43] Y. Zhou, Q. Bao, L.A.L. Tang, Y. Zhong, K.P. Loh, *Chem. Mater.* 21 (2009) 2950–2956.
- [44] G.Q. Luo, X.J. Jiang, M.J. Li, Q. Shen, L.M. Zhang, H.G. Yu, *ACS Appl. Mater. Interfaces* 5 (2013) 2161–2168.
- [45] L.Y. Liang, H.M. Liu, W.S. Yang, *Nanoscale* 5 (2013) 1026–1033.
- [46] M.S. Zhu, P.L. Chen, M.H. Liu, *J. Mater. Chem.* 22 (2012) 21487–21494.
- [47] J. Gao, F. Liu, Y. Liu, N. Ma, Z. Wang, X. Zhang, *Chem. Mater.* 22 (2010) 2213–2218.
- [48] H. Wang, J.T. Robinson, X. Li, H. Dai, *J. Am. Chem. Soc.* 131 (2009) 9910–9911.
- [49] X.Y. Zhang, H.P. Li, X.L. Cui, Y. Lin, *J. Mater. Chem.* 20 (2010) 2801–2806.
- [50] P.H. Wang, Y.X. Tang, Z.L. Dong, Z. Chen, T.T. Lim, *J. Mater. Chem. A* 1 (2013) 4718–4727.
- [51] M. Shah, K. Zhang, A.R. Park, K.S. Kim, N.G. Park, J.H. Park, P.J. Yoo, *Nanoscale* 5 (2013) 5093–5101.
- [52] L. Tong, Z. Li, T. Zhu, H. Xu, Z. Liu, *J. Phys. Chem. C* 112 (2008) 7119–7123.
- [53] K.S. Novoselov, A.K. Geim, S.V. Morozov, D. Jiang, Y. Zhang, S.V. Dubonos, I.V. Grigorieva, A.A. Firsov, *Science* 306 (2004) 666–669.
- [54] S.Q. Liang, J. Zhou, X.L. Zhang, Y. Tang, G.Z. Fang, T. Chen, X.P. Tan, *Crystengcomm* 15 (2013) 9869–9873.
- [55] M.W. Shao, L. Lu, H. Wang, S. Wang, M.L. Zhang, D.D.D. Ma, S.T. Lee, *Chem. Commun.* 23 (2008) 2310–2312.
- [56] H.W. Chen, Y. Ku, Y.L. Kuo, *Chem. Eng. Technol.* 30 (2007) 1242–1247.
- [57] Q.J. Xiang, J.G. Yu, M. Jaroniec, *Nanoscale* 3 (2011) 3670–3678.
- [58] W.B. Hou, Z.W. Liu, P. Pavaskar, W.H. Hung, S.B. Cronin, *J. Catal.* 277 (2011) 149–153.
- [59] Z. Ji, X. Shen, J. Yang, G. Zhu, K. Chen, *Appl. Catal. B* 144 (2014) 454–461.
- [60] Y. Li, X. Li, J. Li, J. Yin, *Water Res.* 40 (2006) 1119–1126.
- [61] X.F. Zhou, C. Hu, X.X. Hu, T.W. Peng, J.H. Qu, *J. Phys. Chem. C* 114 (2010) 2746–2750.
- [62] Y.Q. Yang, G.K. Zhang, S.J. Yu, X. Sheng, *Chem. Eng. J.* 162 (2010) 171–177.
- [63] Y.Y. Li, J.S. Wang, H.C. Yao, L.Y. Dang, Z.J. Li, *J. Mol. Catal. A: Chem.* 334 (2011) 116–122.
- [64] J. Jiang, L.Z. Zhan, *Chem. Eur. J.* 17 (2011) 3710–3717.
- [65] L. Kuai, B.Y. Geng, X.T. Chen, Y.Y. Zhao, Y.C. Luo, *Langmuir* 26 (2010) 18723–18727.
- [66] X. Wang, S. Li, H. Yu, J. Yu, S. Liu, *Chem.: Eur. J.* 17 (2011) 7777–7780.
- [67] Y.P. Liu, L. Fang, H.D. Lu, L.J. Liu, H. Wang, C.Z. Hu, *Catal. Commun.* 17 (2012) 200–204.
- [68] Y.Y. Wen, H.M. Ding, Y.K. Shan, *Nanoscale* 3 (2011) 4411–4417.
- [69] J.G. Yu, J.F. Xiong, B. Cheng, S.W. Liu, *Appl. Catal. B* 60 (2005) 211–221.
- [70] Q. Xiang, J. Yu, M. Jaroniec, *Chem. Soc. Rev.* 41 (2012) 782–796.